# Viscous fingering in square-lattice models with two types of bonds

Unni Oxaal, Finn Boger, Jens Feder, and Torstein Jøssang
*Department of Physics, University of Oslo, Box 1048 Blindern, N-0316 Oslo 3, Norway*

Paul Meakin
*Central Research and Development, E. I. du Pont de Nemours and Company, Wilmington, Delaware 19880-0356 and Department of Physics, University of Oslo, Box 1048 Blindern, N-0316 Oslo 3, Norway*

Amnon Aharony
*Raymond and Beverly Sackler Faculty of Exact Sciences, School of Physics and Astronomy, Tel Aviv University, Tel Aviv 69978, Israel and Department of Physics, University of Oslo, Box 1048 Blindern, N-0316 Oslo 3, Norway*

(Received 8 July 1991)

Immiscible two-fluid displacement was studied experimentally and numerically in inhomogeneous porous models. Square-lattice models were designed using bond percolation. A fraction $f$ of the bonds was randomly given a high permeability, set equal to 1. The rest $(1-f)$ have a low permeability ($\kappa=0.004$). The patterns formed by the displacement of glycerol by air injected at the center of the model network were studied and compared with the results of diffusion-limited-aggregation (DLA) simulations on model bond networks that correspond precisely to the experimental models. We studied models with fractions of good bonds close to the threshold value for bond percolation $f_c=0.50$. Experimental results are well represented by simulations and can be characterized by the same effective fractal dimension $D_c \simeq 1.5$. We find that the model geometry strongly influences formation of the displacement pattern, and that the results are *independent* of $f$. Unlike usual DLA aggregates, which grow mainly at the tips, the geometry of our models causes growth in the interior, yielding a gradual increase of the effective fractal dimension as the aggregate grows.

PACS number(s): 47.55.Mh, 47.55.Kf, 68.70.+w, 05.40.+j

## I. INTRODUCTION

A wide variety of ordered and disorderly patterns are generated during fluid flow processes. An important class of examples is the formation of displacement fronts when one fluid displaces another in a porous medium. Developing a quantitative understanding of the evolution of these fluid-fluid interfaces is of considerable interest and can have important practical implications for oil recovery, hydrology, and materials processing. These displacement fronts often have a complex random structure that can be described quite well in terms of fractal geometry [1]. Within this class alone a broad range of displacement patterns can be formed depending on the displacement rate, fluid rheologies, miscibility, interfacial tension, the structure and wetting properties of the porous medium, as well as other factors such as gravity [2,3]. While substantial progress has been made towards the objective of describing these displacement patterns, we are still far from a general understanding, and new phenomena are still being discovered and recognized. For fluid-fluid displacement in a porous medium, geometric and chemical heterogeneities on a wide range of length scales play an important role that is not well understood. Under some conditions fractal displacement fronts are formed that can be described (at least in part) in terms of simple models such as invasion percolation [4–6] (slow displacement of a wetting fluid by a nonwetting fluid) or diffusion-limited aggregation [7] (fast displacement of a high-viscosity fluid by a low-viscosity fluid) [8–11].

While our ultimate goal is to develop a comprehensive theoretical understanding of fluid-fluid displacement phenomena, this goal may not be obtainable in the foreseeable future. An important intermediate step is to find ways of describing these processes in terms of simple computer models such as invasion percolation, Eden growth [12], and diffusion-limited aggregation (DLA). This approach has proven to be quite successful during the past decade or so. Here we describe a detailed comparison between the results of fluid-fluid displacement experiments carried out using pseudo-two-dimensional porous media with controlled disorder, and the results of computer simulations carried out using a modified DLA algorithm [13] on the *same* models. We believe that such comparisons are important to determine to what degree current models represent the behavior of real systems and to stimulate the development of improved models.

Viscous flow of a fluid in a porous medium is described by Darcy's law that (neglecting gravity effects) states that the fluid flux is proportional to the pressure gradient in the viscous fluid being displaced. For incompressible fluids the divergence of the velocity vanishes and Darcy's equation leads to the Laplace equation $\nabla^2 P=0$ for the pressure field in the fluid, if the permeability is constant.

Displacement of one fluid by another is a more com-

 

plex process and the description traditionally used in reservoir simulations uses a set of generalized Darcy's equations that assume steady, decoupled simultaneous flow of the two fluids [14]. This assumption is not correct for the present experiments since we consider a moving displacement front.

Complex fingerlike instabilities (viscous fingers, VF) in the displacement front arise at high displacement pressures. Oxaal *et al.* [15] studied VF on a percolation model that contained a fraction $f=f_c=0.50$ of identical open bonds between pores on a square lattice. At this critical concentration, the flow was constrained to the backbone of the fractal spanning cluster and the resulting fingers had a fractal dimension 1.3.

Recently, Meakin *et al.* [13] considered a modified DLA algorithm. They studied the scaling properties of DLA aggregates on square-lattice models where all bonds were randomly assigned one of two permeabilities. Based on numerical results they suggested a crossover scaling form that was a function of the ratio $\kappa$ of the bond permeabilities and of the fraction $f$ of high-permeability bonds in the model.

Oxaal [16] compared in detail experiments and such modified DLA simulations on a "two-permeability" model with $f\simeq 0.50$ and $\kappa=0.004$. The experimental displacement patterns in these two-permeability models were strikingly different from experiments on regular square-lattice models, and from experiments on the percolation model. The pore-space geometry influenced formation of the displacement pattern strongly, and the essential features of the experimental observations were reproduced in the simulations.

In this paper we explore the effect of changing the fraction $f$ of good bonds close to the critical value for bond percolation $f_c=0.50$. In part, this is done to test the scaling theory of Meakin *et al.* [13], which predicted a clear crossover from the behavior observed [15] at $f=f_c$ and $\kappa=0$ to that on a regular lattice. As $f$ is changed in ordinary percolation, the cluster structure changes rapidly. We expected that the structure of the patterns formed during displacement would depend on $f$. We used four values $f=0.45$, 0.48, 0.50, and 0.52 and fixed the ratio between the permeability of weak and good bonds at $\kappa=0.004$. All experiments and most simulations lie in a regime that has not been studied before.

Our results show that the transport properties of the models do not depend (apart from a change in global permeability) on the fraction of good bonds $f$, at the permeability ratio $\kappa$ studied. The weak bonds contributed significantly to fluid transport, even when they were not essential to obtain a connected path from source to sink. At $f=0.52$ the paths invaded by air included weak bonds although alternative routes through good bonds existed, and at all our values of $f$ branches were invaded that would be "dead ends" without the presence of weak bonds.

The type of network we describe in this paper should also be relevant for macroscopic flow in inhomogeneous media such as regions of high-permeability rock embedded in low-permeability rock, or fractured (low-permeability) rock.

## II. EXPERIMENT

### A. Model geometry

We made square-lattice models of size $L\times L$ with uniform cylindrical pores on each node. We used $L=145$, and assigned random numbers uniformly distributed between 1 and 100 to the *bonds*. The same $292\times 292$ matrix of random numbers was used for all models. We used the numbers to construct four models that had different fractions $f$ of good bonds. We chose a clipping level, all bonds with numbers below this level got high permeability, and bonds with numbers at and above this clipping level got low permeability. We used four clipping levels; 52, 50, 48, and 45. For the set of random numbers we used, the fractions $f$ we obtained were 0.5179, 0.4969, 0.4771, and 0.4492, but we will use the rounded (nominal) values for $f$ to identify the models. This way of constructing the models ensured that all good bonds present in the model $f=0.45$ were present in models with higher values of $f$.

In analogy with ordinary bond percolation we define clusters to be groups of pores connected by *good* bonds. One good bond connecting two pores (sites) will be called a cluster of size two, and $s$ pores connected by good bonds will be called a cluster of size $s$. To characterize a *given* model we define a correlation length $\xi_l$ that is an average distance between two pores connected through good bonds. In taking this average we sum over all clusters in the model including those with pores at the boundary. Usually clusters that include boundary sites

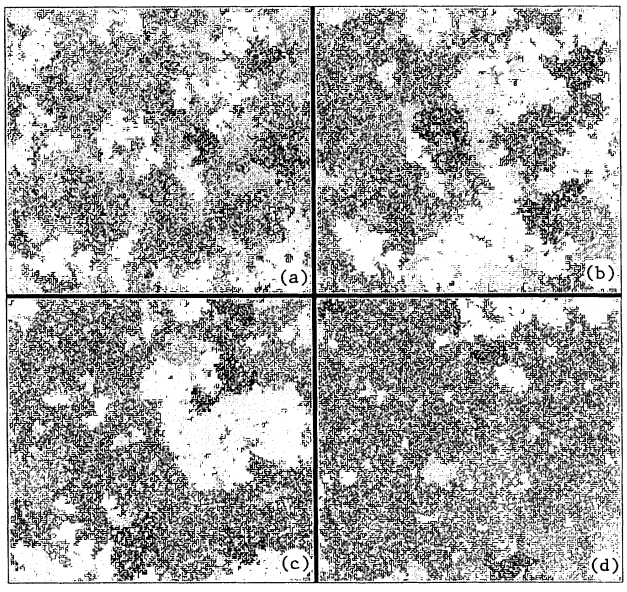


FIG. 1. Clusters of pores connected by good bonds are shown in different shades of gray. The local correlation length is of the same size as a "typical" cluster. (a) The model with fraction $f\simeq 0.45$ of good bonds, (b) the $f\simeq 0.48$ model, (c) the $f\simeq 0.50$ model, and (d) the $f\simeq 0.52$ model.

TABLE I. Geometrical characteristics of the four models. The correlation lengths are in units of the lattice constant $a=1.9$ mm. The percolation threshold for bond percolation on the square lattice is $f_c=0.5$.

| Model | Bond concentration $k=1$ $f$ | Correlation length good bonds $\xi_l$ | Measured permeability ratio $\kappa$ |
|---|---|---|---|
| 52 | 0.5179 | 52.3 | $4\times10^{-3}$ |
| 50 | 0.4969 | 25.4 | $4\times10^{-3}$ |
| 48 | 0.4771 | 21.92 | $4\times10^{-3}$ |
| 45 | 0.4492 | 10.38 | $3\times10^{-3}$ |

are discarded, since they are truncated by the boundary and their shape is not representative. We chose to include them when $f\leq f_c$ since we focused on the structure formed by clusters of pores that we expected to dominate the fluid transport from the center to the boundary. In the model with $f\simeq0.52$, the spanning cluster was not included in the average, and $\xi_l$ is the typical size of finite clusters, or of the holes in the spanning cluster. Figure 1 shows clusters of pores connected by good bonds for the four experimental models in this paper. Table I gives $\xi_l$ for the four models.

### B. Experimental procedures

Experimental procedures were described in detail in an earlier paper by Oxaal [16]. Here we give a brief outline.

Physical models were made by a photolithographic technique using a computer generated mask whereby we obtained a recessed pattern of pores connected by bonds. We made models as described above with four values of $f$. A "lid" was clamped over the pattern so that fluid flow was only possible on the etched network. The network was filled with dyed glycerol that later was displaced by centrally injected air at constant pressure. While air intruded, a growing structure of air-filled pores and bonds was photographed from above at regular intervals. When the intruding air reached the boundary of the model the experiment was stopped. After digitizing the negatives we identified the coordinates of drained pores in the aggregate, could find the scaling relations as described in Sec. III A, and compared experimental with simulated aggregates in detail.

The capillary number defined by $\mathrm{Ca}=\mu_2 U/\sigma$ is a controlling parameter in the experiment. Here $\mu_2$ is the viscosity of the displaced fluid, $U$ is the average front velocity, and $\sigma$ the surface tension. The capillary number expresses the balance between viscous forces and capillary forces. We determined the capillary number Ca as described by Oxaal [16]. The maximum capillary number used in the experiments was $\mathrm{Ca}\simeq0.12$ ($f\simeq0.50$) and the minimum value was $\mathrm{Ca}\simeq0.05$ ($f\simeq0.52$). In our experiments $\log_{10}(\mu_1/\mu_2)=-4.3$, where $\mu_1$ is the viscosity of the injected fluid, and $\mathrm{Ca}\geq0.03$, falling within the viscous fingering domain, according to Lenormand, Touboul, and Zarcone [11]. In this domain viscous forces dominate and DLA is expected to be an appropriate model.

### C. Simulations

In the DLA model of Witten and Sander [7] particles are added, one at a time, to a growing aggregate. We use a modified DLA algorithm introduced by Meakin *et al.* [13] that takes the two bond permeabilities into account. It was further modified so that we could "feed" the coordinates of weak and good bonds used in experiments to the program. The algorithm is described in detail in the work of Meakin *et al.* [13], and a compact description is given by Oxaal [16].

The algorithm requires large amounts of computer time compared to standard DLA simulations, but it is fast and simple compared to solving flow equations on a network.

## III. RESULTS

In the first two subsections we present experimental results in conjunction with simulations where weak and good bonds were placed at exactly the same coordinates as in the experimental models, and with the values of $f$ and $\kappa$ as in the experiments. We call such simulations "simulations on the experimental model." In the next subsection we describe an experiment and a set of simulations where the permeability ratio $\kappa$ was changed compared to the previous systems, and in the last subsection we present results of simulations on other model realizations, but where $\kappa$ and $f$ have the same value as in the experimental systems.

### A. Experiments and "simulations on the experimental model"

Figure 2 shows a photograph of an experiment at a given instant $t$. By analyzing the digitized picture we found both the total mass $M_0(t)$ and the radius of gyration $R_g(t)$. By repeating this procedure for a sequence of photographs of a given experiment, we obtained $M_0(R_g)$ as a function of $R_g(t)$. We did this for experiments on four models with fractions $f\simeq0.45$, 0.48, 0.50, and 0.52 of good bonds. Black dots in Fig. 3 show the result of analyzing such sequences of pictures for each $f$.

We found that the displaced mass increased algebraically with the radius of gyration:

$$M_0\sim R_g^{D_g}\ . \tag{1}$$

The exponent $D_g$ is called *the radius of gyration dimension* [17]. It is a noninteger number less than the spatial

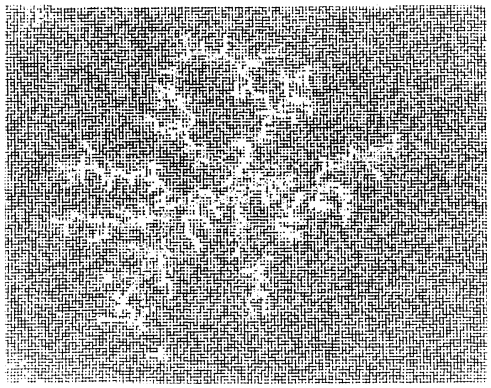

FIG. 2. The model with $f \simeq 0.48$. Fluid flow is only permitted on the recessed network of pores and connecting bonds that appear black when filled with dyed glycerol. Air injected through the central site has displaced glycerol, and these sites and bonds appear white.

dimension $d=2$ (see the caption of Fig. 3, and Table II). The function $M_0(R_g)$ compares different stages of the growth in an experiment or a simulation. We estimate the error in all the dimensions found in this section to be $\pm 0.1$. The main source of the error comes from different possible ranges of the points that are included in the linear log-log fits.

The total mass $M_0$ and the radius of gyration $R_g$ represent only a single global property of a specific finite aggregate. A more detailed characterization of the aggregate is given by the function $M(R)$, which means the cumulative mass of the aggregate within circles of successively increasing radii $R$ centered at the site of injection. Plotting $M(R)$ versus $R$ we obtained a power-law dependence, with a noninteger exponent $D_c$, called the *cluster dimension* [17]. This function is easy to measure and gives a robust measure of the scaling property of a *given* structure.

Each curve in the plots of Fig. 3 was generated from a digitized photograph taken during the displacement ex-

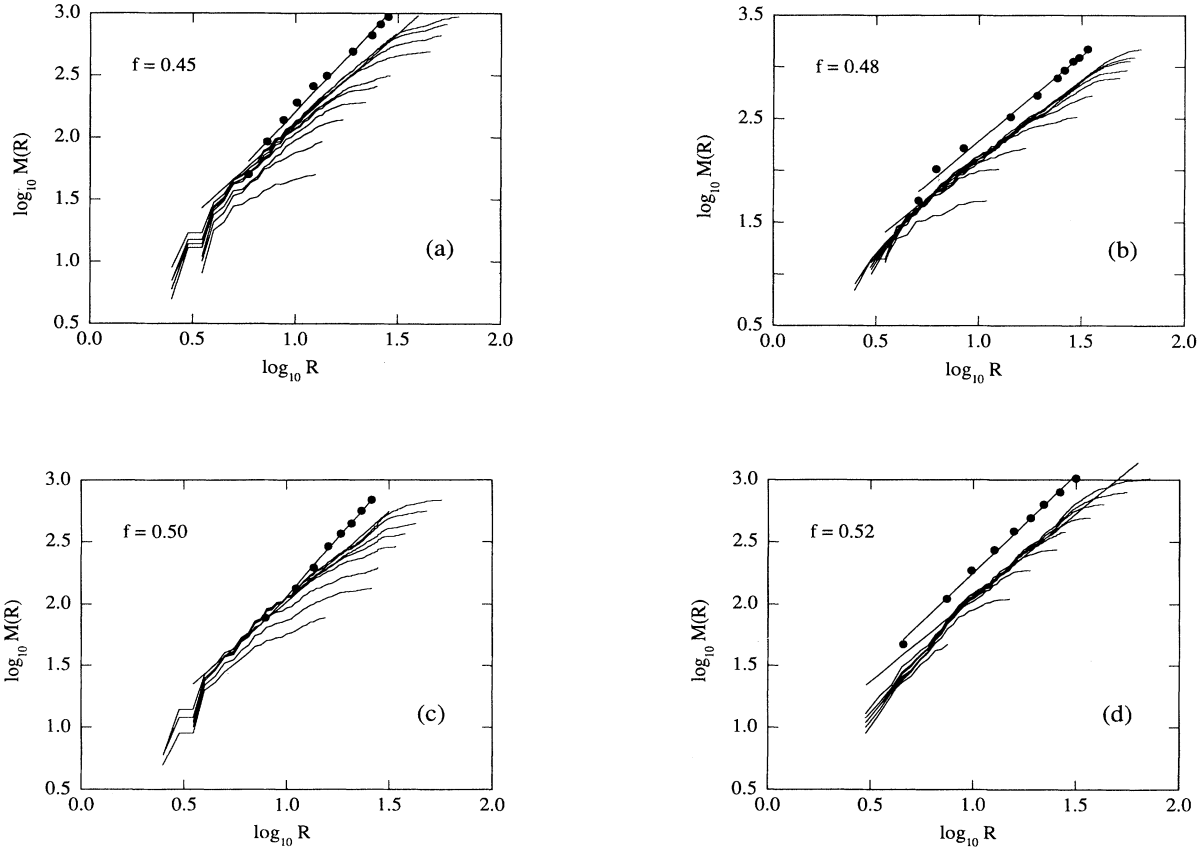


FIG. 3. *Experiment.* In each figure, each curve shows the dependence of $\log_{10}M(R)$ on $\log_{10}R$ at a particular stage in the displacement. $M(R)$ is the cumulative mass within circles of increasing radius $R$. Straight lines fitted to the last stage of each set of curves have a slope $D_c$. A black dot corresponding to each curve shows the logarithm of total aggregate mass $M_0$ at that stage placed at the logarithm of radius of gyration $R_g$ of that stage of the aggregate. Straight lines fitted to the black dots have a slope $D_g$. Plots (a)–(d) represent experiments with $f \simeq 0.45$, 0.48, 0.50, and 0.52. The abscissa should be interpreted as $\log_{10}R_g$ for the black dots, and as $\log_{10}R$ when considering the set of curves. The values of $D_c$ and $D_g$ are (a) $D_c=1.5$ and $D_g=1.8$, (b) $D_c=1.5$ and $D_g=1.7$, (c) $D_c=1.5$ and $D_g=1.9$ and (d) $D_c=1.6$ and $D_g=1.6$.

TABLE II. The *overlap* between two aggregates is the number of pores that are common to both, divided by the number of pores invaded by the least massive aggregate (see text). The average aggregate mass varies with the concentration of high-permeability bonds $f$. The numbers given are the average of all possible pairs within a group (such as ten combinations of an experiment with ten simulations on the same model). The uncertainties in the overlap are all $\pm 0.05$ and reflect the scatter in the overlap values.

| Model | Cluster dimension $D_c$ $\log M/\log R$ | Radius of gyration dimension $D_g$ $\log M_0/\log R_g$ | Overlap experiment-simulation | Overlap simulation-simulation | Overlap experiment-experiment | Overlap different models |
|---|---|---|---|---|---|---|
| 45 | 1.5 | 1.8 | 0.50 | 0.48 | | 0.18 |
| 48 | 1.5 | 1.6 | 0.48 | 0.50 | | 0.16 |
| 50 | 1.5 | 1.9 | 0.57 | 0.52 | 0.75 | 0.16 |
| 52 | 1.6 | 1.6 | 0.56 | 0.52 | 0.76 | 0.16 |
| mean | 1.5 | | 0.53 | 0.51 | | 0.17 |

periment. The lowest curve in each plot represents an early stage of the displacement. Each of the other curves represents a later instant in the same displacement experiment.

The aggregate reaches its total mass $M_0$ at the maximum radius $R_0$ proportional to $R_g$. The function of $M(R)$ is given by the scaling form

$$\frac{M(R)}{M_0} = (R/R_g)^{D_c} F(R/R_g) \ . \tag{2}$$

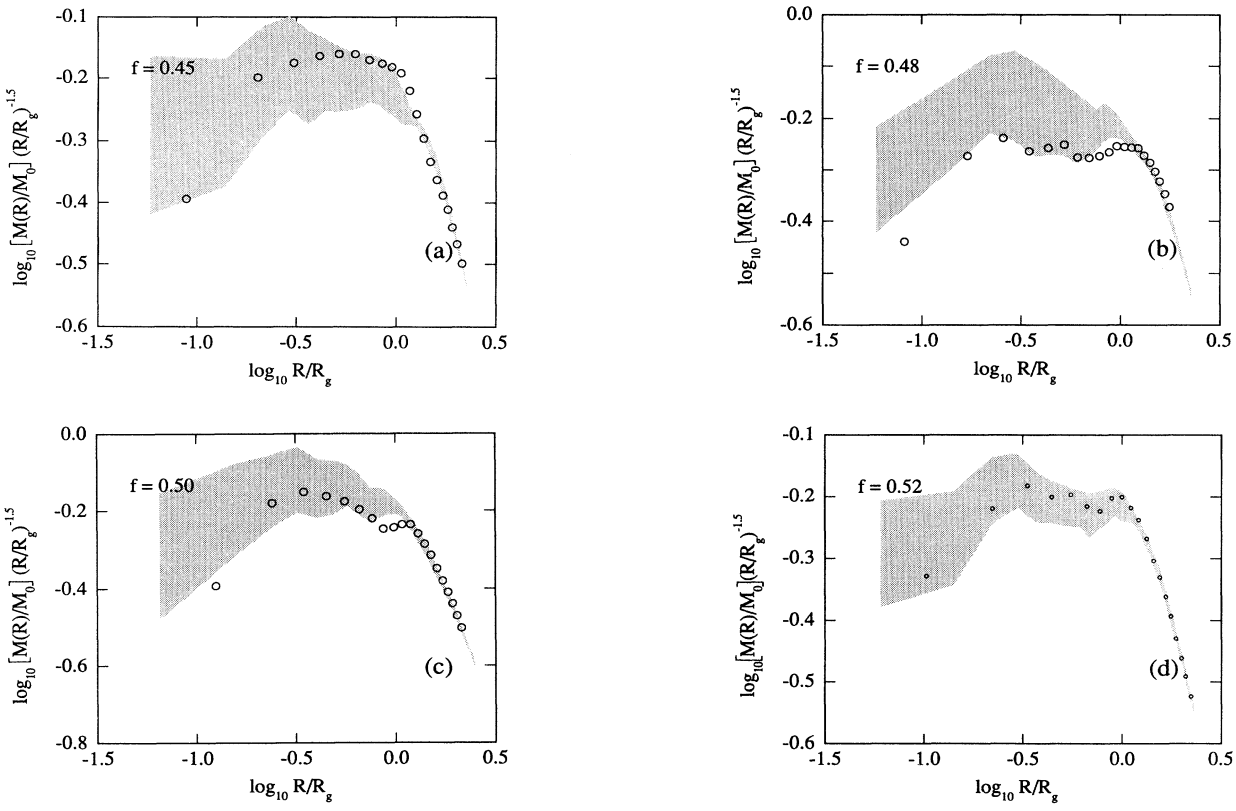


FIG. 4. *Experiment and simulation.* Circles are experimental data showing the normalized mass $[M(R)/M_0](R/R_g)^{-1.5}$ as a function of the normalized radius $R/R_g$ for the last stage of experiments at $f \simeq 0.45$, 0.48, 0.50, and 0.52. The shaded gray region represents ten independent simulations on experimental models. They are averaged, and we only show the rms deviation of the simulations around the average.

Here $x = R/R_g$ is the rescaled circle radius; the scaling function $F(x)$ describes the finite size cutoff. We scale the circle radius with $R_g$ rather than with the maximum cluster radius, since $R_g$ is less sensitive to fluctuations in the aggregate shape.

For structures scaling with an exponent $D_c$, $F(x)$ is constant in the range $x \ll 1$ and decreases as $x^{-D_c}$ for $x \gg 1$, so that $M \to M_0$ as $R \gg R_g$. Open circles in Fig. 4 show $F(x)$ for the last experimental stage before breakthrough. The experimental data are shown together with the rms deviations around the average of ten independent simulations on each of the four experimental models. The simulation results are averaged by coarse graining the data. The abscissa is subdivided into suitable segments, and the average radius and average mass within each segment are found. The standard deviation within each segment is found, and the shaded gray band in Fig. 4 corresponds to one standard deviation from either side of the average of the simulations. The plots emphasize the deviations from scaling at small radii.

In Figs. 3(a) and 3(c), at a *given* value of $R$ the number of pores $M(R,t_1)$ invaded at one time $t_1$ is less than at a later time $t_2$, $M(R,t_1) < M(R,t_2)$. Thus new pores are added to the structure at radii $R(t) < R_g(t)$, and not only at values of $R(t)$ close to $R_{\max}(t)$. Qualitatively we can state that the structures in Figs. 3(a) and 3(c) grow in the interior as well as at the tips. In contrast, tip growth is a well-established characteristic for DLA-like growth on a homogeneous substrate [18].

We superimposed successive stages of the experiment in Fig. 5, where pores added to each interval were assigned a different symbol, and found that the interior

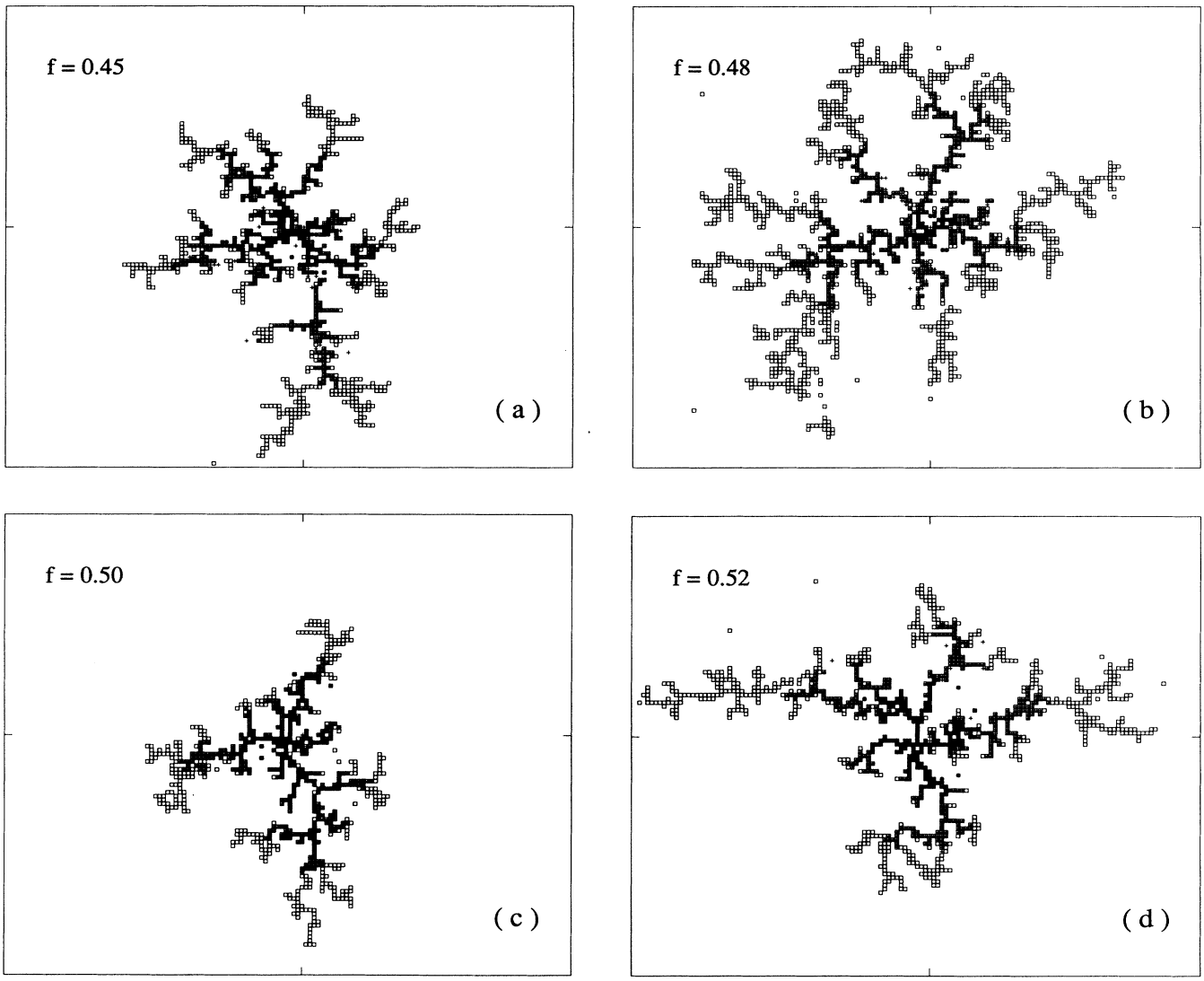


FIG. 5. Three experimental stages superimposed. In each picture, filled squares represent pores drained during the first stage of the experiment, crossed squares represent pores drained during the next stage, and open squares show those pores drained in the following interval. A plus and hatches on the frame show the site of injection. The interval between the stages is (a) $t = 3.52$ s, (b) $t = 3.30$ s, (c) $t = 1.65$ s, and (d) $t = 5.3$ s.

growth was induced by the pore-space geometry. New pores were added predominantly at the tips of the three/four main arms of the aggregate. Some parts of the arms curl back and some smaller arms start out late, and add pores to the aggregate at radii $R < R_g(t)$, producing the "layering" of the curves in Figs. 3(a) and 3(c).

Pores are plotted with a diameter equal to the lattice constant $a$. In the experiments the pore diameter is $a/2$. In a few cases the enlarged plotting symbols create loops in the pictures. No loops were created in the experiments, we have only observed branching structures.

The simulations produced a list of coordinates of sites (pores) belonging to the aggregate, in the order in which they were added. This allowed us to plot the simulations in the same way that experimental data were plotted in Fig. 3. As for the experimental data, these simulation data also approach the $M(R)$ curve for the largest cluster. (These figures are not shown; they look like those in Fig. 3.) The average exponent for ten independent simulations is $D_c \simeq 1.5 \pm 0.1$ independent of the value of $f$.

When experiments showed internal growth, i.e., layered curves when plotting the cumulative mass $M(R)$ versus $R$ for different growth stages, about seven of ten simulations on the experimental model showed internal growth. Conversely, when experiments did not exhibit layering of the $M(R)$ curves, simulations on the experimental model failed to show layering in about seven or eight of ten independent simulations. The simulations on the experimental models thus represent the internal growth correctly in a "statistical" sense.

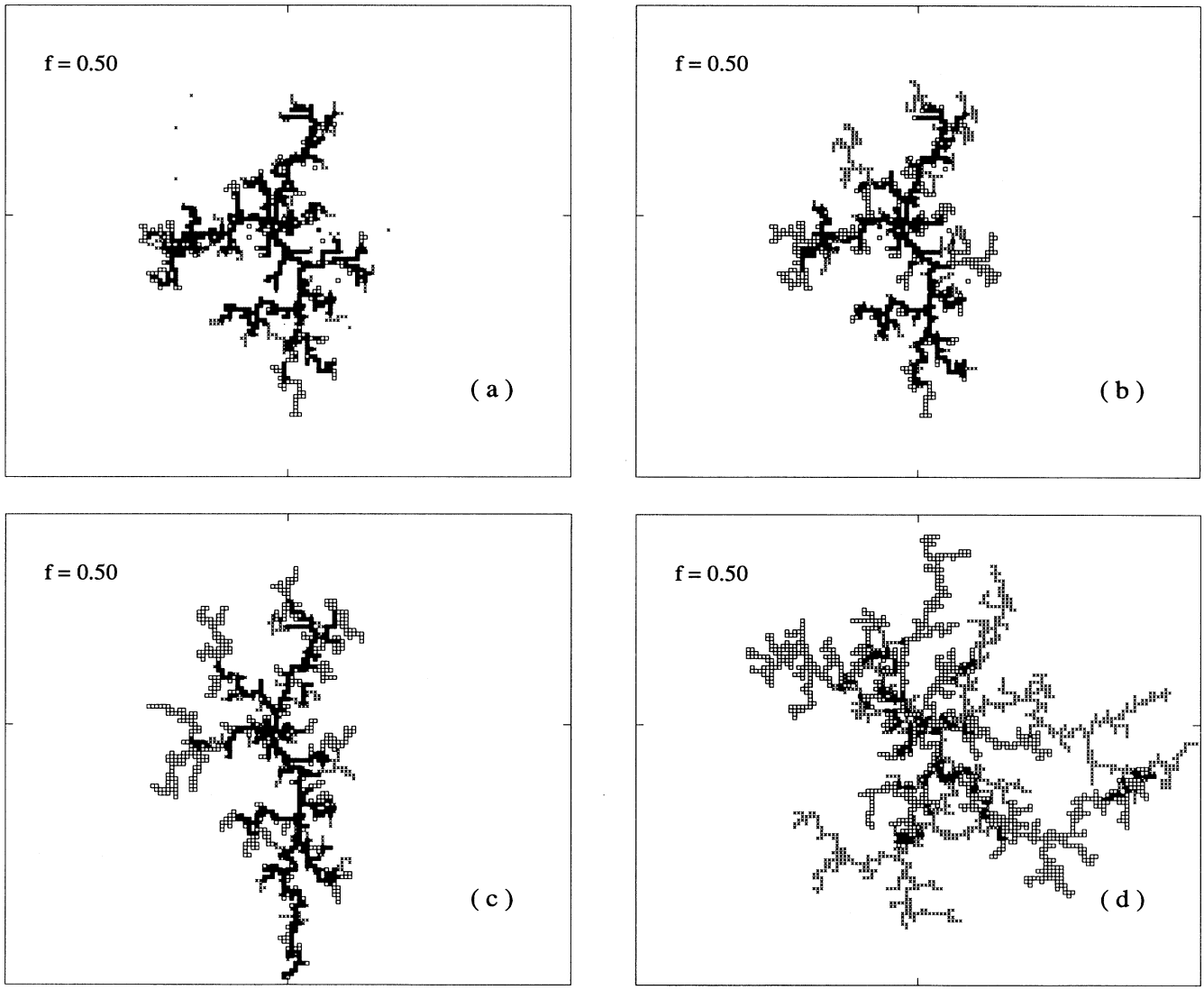


FIG. 6. Cluster overlaps. In each frame, boxes show one aggregate, crosses the other, and crossed boxes pores common to both aggregates. (a) Overlap of two independent experiments in the $f \simeq 0.50$ model, $S_{\text{average}} = 0.75$. (b) Overlap of an experiment and simulation on the experimental model, $S_{\text{average}} = 0.53$. (c) Overlap on two independent simulations on the experimental model, $S_{\text{average}} = 0.51$. (d) Overlap of two independent simulations on independent realization with $\kappa = 0.004$ and $f \simeq 0.50$, $S_{\text{average}} = 0.16$.

### B. Overlap of aggregates

A sensitive quantitative way to compare experiments and simulations involves the amount of *geometrical* overlap between them at the same aggregate mass [15].

We measured overlap between two aggregates (mass $M_1$ and $M_2$) on the same model with the parameter $S = M_{\text{overlap}}/M$, where $M = \min(M_1, M_2)$ and $M_{\text{overlap}}$ is the mass of the pores with coordinates common to both structures (see Table II). When at least one of the aggregates is simulated, $M_1 = M_2$. Overlap between two experiments is not found at a common aggregate mass, since photos cannot be taken at predetermined (and equal) aggregate masses.

Examples of overlaps of pairs of aggregates generated in various ways are shown in Fig. 6. The examples correspond to the four columns of Table II that show $S$.

In experiments, overlap between independent experiments on the same model is high, $S \simeq 0.75$, and well above the overlap between experiments and "simulations on the experimental model," $S = 0.53$. The average overlap between two simulations on a given model ($S = 0.51$) is the same as the average experiment-simulation overlap. The overlap between simulations performed on independent model realizations for given $f$ and $\kappa = 0.004$ was $S = 0.17$. This value gives a feeling for the significance of the overlap in the other cases presented in Fig. 6 and Table II.

### C. Simulations and an experiment in models with other value(s) of $\kappa$

All simulations discussed so far were performed at permeability ratios in the range $\kappa = 0.003 - 0.004$, calculated using the measured bond widths on the physical models on which the flow experiments were performed.

For $f \simeq 0.45$ we performed simulations at other values of the permeability ratio $\kappa$ to test whether experiment and simulations would match even better. We did four independent simulations at each value of the permeability ratio $\kappa = 1$, 0.675, 0.04, 0.004, 0.0004, 0.0001, and 0.000 04. The results are shown in Fig. 7 together with the experiment at $f \simeq 0.45$. At a given $R_g$, experimental data start out with a mass that is lower than in any of the simulated curves. However, the experimental data have a larger increase of mass as $R_g$ grows. As seen in Fig. 7, the experimental data are consistent with the simulations for $\kappa$ in the range 0.004–0.0004, reflecting the low sensitivity of the experimental results to variations in $\kappa$.

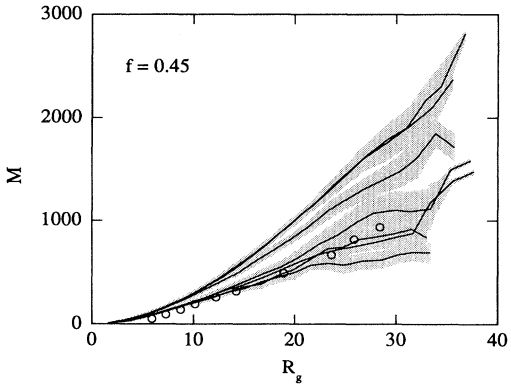


FIG. 7. *Experiment and simulations.* Open circles show the cluster mass $M^{\text{expt}}(t)$ at a given stage of the experiment at $f \simeq 0.45$, vs the corresponding radius of gyration $R_g(t)$. Starting from the top right-hand side of the figure, lines show average simulated masses $M_{\text{sim}}$ as function of $R_g^{\text{sim}}$ at permeability ratios $\kappa = 0.675$, 1, 0.04, 0.004, 0.0001, 0.0004, and 0.000 04. The standard deviation of the simulations around each average is represented by the shaded gray area.

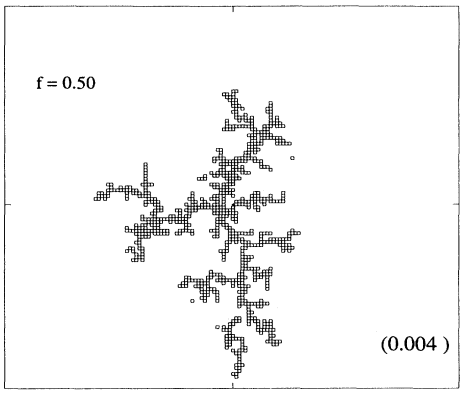


FIG. 8. A displacement experiment in a new model with $f \simeq 0.50$ and $\kappa = 0.04$. The average overlap with the experiments at $\kappa = 0.004$ is $S = 0.73$.

Recently, we have performed an experiment in a new model at $f \simeq 0.50$, with $\kappa = 0.04$ (a factor of 10 higher than in the present series), but with the *same* coordinates for good and weak bonds (see Fig. 8). This model also has considerably less scatter in the bond widths than before, since we now can draw the masks at four times the previous resolution. With the method used to measure bond widths [16], we are not able to detect fluctuations in bond widths.

Comparing this experiment with the other experiments at $f \simeq 0.50$, the displacement pattern on the new model strongly resembles patterns formed on the old model ($f \simeq 0.50$ and $\kappa = 0.004$). The overlap between new and old experiments is $S = 0.73$. We also did experiments at $\kappa = 0.4$, and they showed displacement patterns with preferential growth along the network axes leading to a distinctly anisotropic pattern of ramified viscous fingers. The pattern envelope has approximately fourfold symmetry.

### D. Simulation results on other models with $f$ and $\kappa$ values equal to experimental models

Figure 9 shows simulations on models at $f \simeq 0.52$ and $\kappa = 0.004$ that are not identical to the experimental model. The top figure shows an average over nine models with four independent simulations on each. The middle and lower plots show two separate sets of four independent simulations, each set on a different model. All plots show the crossover function $F(x)$ of Eq. (2), and although the average (over many realizations) $F(x)$ is constant for $x < 1$ as expected theoretically, we observed a model-dependent shape when we separate simulations on individual models.

We have 58 independent simulations on ten model realizations of size $145\times145$ sites at $f\simeq0.50$, $\kappa=0.004$. For $f\simeq0.45$, 0.48, and 0.52 we have 46 simulations at $\kappa=0.004$. At each value of $f$, averaging over all simulations, we find an exponent $D_c=1.6\pm0.1$ independent of $f$.

Figure 9 is typical of what we observed at the four values of $f$: The crossover function has a distinct shape on individual models.

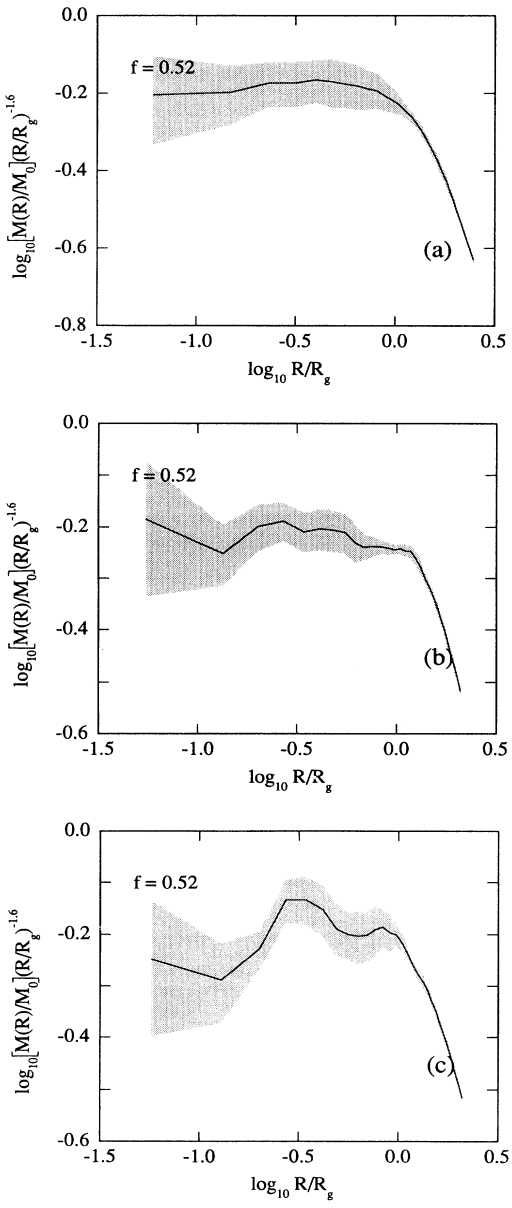


FIG. 9. *Simulation.* The normalized number of pores $[M(R)/M_0](R/R_g)^{-1.6}$ as a function of the normalized radius $R/R_g$ for simulations at $f\simeq0.52$ and $\kappa=0.004$. Lines show average values, the shaded gray regions represent the rms deviation of the simulation around the average. (a) Average of 36 independent simulations on nine *different* models. Each model is a different realization of the case $f\simeq0.52$. (b) Average and standard deviation for four independent simulations on *one* model. (c) Average and standard deviation for four independent simulations on *another* model.

Simulations on two larger models of $401\times401$ sites with $\kappa=0.004$ at each value of $f$ were also performed, and as for the $145\times145$ models we found that the model geometry influences the shape of the crossover function $F(x)$ at length scales $R<R_g$. For $f=0.52$ the difference in shape is not very distinct. The two models we tested showed differences at short length scales up to $\log_{10}(R/R_g)=-0.8$, a different behavior around crossover to finite size, and a different level of the constant plateau. Again, we found an average $D_c\simeq1.6\pm0.1$.

## IV. DISCUSSION

In this section we discuss the main quantities measured, i.e., the overlap of pairs of aggregates and the scaling of aggregates. We compare these quantities for aggregates generated in different manners and discuss the influence of changing the fraction of good bonds $f$.

### A. Overlap

From the overlap data collected in Table II, we conclude that the underlying geometry of the pore space *strongly* influences the growth of both the viscous fingers and the simulations, and that the overlap does not depend on the fraction $f$ of good bonds, in the range of $f$ studied.

On a specific model, the overlap between an experiment and a simulation or between two simulations is significantly lower than the overlap between two experiments. Thus the simulations are not as reproducible as experiments, they are more "noisy."

Despite the instability of the displacement process, the experiments show a high degree of overlap. We believe that an "ideal" viscous fingering experiment in these model geometries would be almost deterministic: The permeability fluctuations, fixed and preset by the exact layout of weak and good bonds, dominate over other possible sources of fluctuations in an ideal experiment and must exert the same influence in every repetition of the experiment.

It might be possible to improve the agreement between the experiments and simulations by including noise reduction to control fluctuations in the simulations.

The real viscous fingering experiments take place on a physical random network with errors in the bond shape and bond widths. Even when the underlying pore-space geometry is set to be the same, different runs of the experiment involve wettability fluctuations, specks of dust, and occasional trapped air bubbles. These errors are randomly distributed, add noise to the experiment, and possibly account for the experiment-experiment overlap being incomplete. The experiment in Fig. 8 on another etching with weak and good bonds in the same positions but with a higher $\kappa$ and less errors demonstrated that the implanted network pattern of weak and good bonds dominates the experimental aggregate formation, and that the errors mentioned above play a minor role. This experiment also showed that variation with $\kappa$ from 0.004 to 0.04 had a small effect on the overall structure of the VF cluster.

Simulations were performed on idealized models,

where all weak and good bonds had their assigned (exact) permeabilities. DLA-like simulations are the result of an interplay between two types of randomness: The random walk that is a sample of the diffusion probability field, and the frozen random structure of the network. The interplay between the two random contributions is not fully understood. Nevertheless, the overlap of independent simulations on the same network is quite high, and we conclude that the frozen randomness of the network dominates aggregate formation in these simulations for the values of $\kappa$ used, and that the lower reproducibility in the simulations is caused by the added stochastic elements.

Meakin *et al.* [13] studied the overlap of simulations at $f_c$ on specific models and found strong similarities, and an increasing overlap as the permeability ratio $\kappa$ was reduced. We interpret their results as follows: When the fluctuations in the medium are increased (by increasing the contrast between weak and good bonds) the overlap increases because the influence of the other stochastic elements in the algorithm becomes even less important compared to the medium.

For $\kappa=0$, Oxaal *et al.* [15] found an even larger overlap between experiment and simulation, $S\simeq 0.75$. The reason for the high overlap was that the growth was severely constrained to occur on the backbone of the spanning cluster.

### B. Scaling and interior growth

#### 1. Theoretical expectations

Meakin *et al.* [13] described the dependence of the aggregate mass $M$ on a characteristic length $R$ by the scaling form

$$M(R)\sim R^{D_2}G(R/\xi,R/L_\kappa)\ . \tag{3}$$

The exponent $D_2=1.3$ is the fractal dimension associated with DLA on an infinite cluster at the percolation threshold [15,19], $\xi\sim(f-f_c)^{-\nu}$ is the usual percolation connectedness correlation length as a function of the fraction $f$ of good bonds, $f_c$ is the percolation threshold fraction of good bonds on the square lattice, and $\nu=\frac{4}{3}$ is the correlation length exponent [20]. $L_\kappa$ is a length set by the bond permeability ratio $\kappa$,

$$L_\kappa\sim\kappa^{-\alpha}\ , \tag{4}$$

and $\alpha$ is a crossover exponent. $G(x,y)$ is a crossover function that describes how the fractal behavior changes from that of DLA on a percolation cluster at $f_c$ to $M\sim R^{D_1}$ (with $D_1=1.7$) of DLA on a homogeneous model as the pore space changes from a percolative geometry to a uniform one by an increase in $\kappa$ or $f$ or both. Meakin *et al.* [13] confirmed Eq. (3) by averaging over many simulations, and found that $\alpha\simeq 0.25$, implying a rather slow variation with $\kappa$.

Qualitatively, $L_\kappa$ is the path length along good bonds that represents the same viscous pressure drop in the viscous fluid as one bad bond. $L_\kappa$ must change from infinity to one as $\kappa$ increases from zero to one.

Meakin *et al.* [13] discussed the form of $G(x,y)$ in some limiting cases: As $\kappa\to 0$ the length scale $L_\kappa\to\infty$ and for $f=f_c$ we have scaling of DLA on a percolation cluster [19,15]. As the fraction $f$ of good bonds changes away from $f_c$, the correlation length $\xi$ decreases and will eventually become less than the model size $L$. On length scales $R<\xi$ the aggregate mass will scale as if on a percolation cluster with an exponent $D_2=1.3$, whereas at length scales $R\gg\xi$ the model will be homogeneous and the aggregate mass should scale with $D_1=1.7$.

Thus, provided that $\kappa\ll 1$ and $\xi$ is in the range $a<\xi<R_g<L<L_\kappa$, a crossover in the scaling of $M$ as a function of size from $D_2=1.3$ to $D_1=1.7$ is expected. As the permeability ratio $\kappa$ increases the associated length $L_\kappa$ decreases, i.e., the contribution from weak bonds to transport properties of the model increases. As $\kappa\to 1$ the scaling behavior on the homogeneous model, $M\sim R^{D_1}$ with $D_1=1.7$ is expected, independent of $f$.

#### 2. Interpretation of results

Even though the present experiments are close to the limit of what we may achieve in practice today, the range of length scales available in these model systems is limited to $0.4\le\log_{10}R\le 1.8$, as discussed in Ref. [16]. To establish a power-law behavior, at least an order of magnitude in the argument is needed. An even larger range may be required to determine crossover behavior. To distinguish the different scaling regimes and the crossover between them, as expected from theory, we need a large range of length scales, so that the various characteristic lengths are well separated. We would like to have $a<\xi<R_g<L_\kappa<L$, where each length scale is separated from its neighbors by one order of magnitude or more. With the available range of length scales, we cannot distinguish crossover behavior. However, since we have a record of how the structure develops, we can extrapolate the effective exponents of the experimental and simulated aggregates from the asymptotic approach of $M(R)$ curves for early stages to the $M(R)$ curve for the last stage, as shown for experiments in Fig. 3. The data in Figs. 3 and 4 show that aggregates scale with an *effective* cluster dimension [Eq. (2)] $D_c=1.5\pm 0.1$ that lies between the theoretical limits $D_1=1.7$ and $D_2=1.3$. The value of $D_c$ does not depend on the imposed variation in $f$.

For simulations, the value of the effective cluster dimension found in this way is further confirmed by averages taken over many models with $f$ and $\kappa$ values similar to the experimental values, and by simulations on $401\times 401$ models. Here we obtained $D_c=1.6\pm 0.1$, in good agreement with the value found on the experimental models. The effective cluster dimension $D_c$ characterizes the *geometric* properties of the aggregates. Reanalyzing the simulation results of Meakin *et al.* [13] ($L=401$, $\kappa=0.002$ and $f\simeq 0.50$) for aggregate sizes comparable to those of the present experiments and simulations, we also find $D_c=1.6$.

#### 3. $D_g$ and interior growth

Our results show that the radius of gyration exponent $D_g$ should be used with some care, since aggregates that show internal growth give large values of $D_g$. In Sec. III A we defined interior growth as mass added to the ag-

gregate at radii $R < R_g(t)$ at times later than time $t$. Obviously, $M$ increases irrespective of where the new mass is added, but $R_g$ can have a very slow growth when mass is added in the interior of the aggregate, and $D_g$ can become larger than the $D_c$ for the full-grown cluster. The interior growth seems to be a natural part of the crossover behavior from an effective fractal dimension of $D_2$ at small radii to $D_1$ at large radii.

Figures 3(a) and 3(c) show this effect. Each point $M(R_g)$ corresponds to an $M(R)$ curve, since the total cluster mass is plotted at the radius of gyration $R_g$. The slope of the $M(R_g)$ curve fitted to these data points is steeper than the curve $M(R)$ for the last stage. We have encountered simulations with strong internal growth that gave a value of $D_g$ larger than 2, which is not a meaningful result when viewing $D_g$ as a geometric dimension.

It can be argued that $D_g$ can describe dynamic aspects of the aggregate growth. The $M(R)$ curves of early stages have low slopes, and only subsequent interior growth allows clusters to obtain the final effective scaling exponent $D_c = 1.5$. The crossover from "low-dimensional" growth to more compact growth is not expressed by $D_g$ or $D_c$ of the fully grown clusters, as anticipated by Meakin *et al.* [13]. On the contrary, both these exponents have higher values at small radii than the values found over the whole range of radii. The difference $\Delta = D_g - D_c$ suggested in Ref. [16] measures the *change* in the scaling properties of the aggregate *during* growth.

In contrast to our findings, it has been established that standard DLA simulations grow mainly in an active zone outside $R_g$ [18]. Experimentally, interior growth is observed on two models. Similarly interior growth may or may not be observed in independent simulations on the same model.

As stated in Sec. III A, we find that interior growth is linked to details in the network geometry that sometimes produce favorable paths that break the tendency for outwardly directed growth observed in homogeneous systems, and that permit slow-growing arms in the interior. Simulations are noisy compared to experiments, i.e., due to the random processes inherent in the simulations, sometimes paths that induce interior growth are chosen and sometimes not. Simulations more often have interior growth on those experimental models that show interior growth than on those that do not, indicating that the fluctuations linked to the network geometry dominate over the other unrestricted random choices that are made in the simulations.

#### 4. *Crossover at $R_g$*

The crossover functions $F(x)$ [Eq. (2)] plotted in Fig. 4 show that in the range $R \leq R_g$ experimental data fall almost entirely within one standard deviation around the average of ten independent simulations on the respective models.

We conclude that experiments are well represented by simulations. The conclusion is strengthened by the observation that repeated and independent simulations on other network realizations with the same values of $f$ and $\kappa$ show crossover functions with model-dependent shapes having more pronounced differences than between experiment and simulations on the experimental model. Clearly the detailed structure of the networks influences aggregate growth, also as expressed in details of the scaling at length scales $R \leq R_g$. Simulations on $401 \times 401$ models confirm the behavior found for smaller models.

The work of Meakin *et al.* [13] mainly addressed *average results* obtained from many simulations on different models at the chosen values of $f$ and $\kappa$. This approach does not capture the model-dependent aspects of the growth, such as model-dependent crossover functions and model-dependent interior growth.

### C. Effects of changing $f$

As $f$ is varied, the aggregates *look* different for each model. Each model produces viscous fingering patterns that are characteristic of the model, and that are quite reproducible. For example, the experiment at $f \simeq 0.48$ produced a large aggregate, with five or six main arms that grew symmetrically. Had one arm dominated as in the other models, growth could not have continued that far before breakthrough. Visual differences show that the relative weight of the different paths changes as weak bonds are replaced by good bonds. The differences in appearance are not accompanied by differences in easily measurable quantities such as scaling and overlap.

A crosslike aggregate seems to develop in the experiment at $f \simeq 0.52$. This may indicate that aggregate growth on this model "feels" that the model starts to resemble the homogeneous square lattice. More experiments on other model realizations at $f \simeq 0.52$ and above are needed to confirm this suggestion. If aggregates grown on models at these values of $f$ and $\kappa$ were to show a systematic fourfold symmetry similar to Fig. 5(d), we may then be observing the bounds for where the DLA algorithm can be applied. In that case, this bound need not be symmetric around $f_c$, and will also depend on $\kappa$.

As $f$ was changed, no variation in the effective dimensions and the overlap was observed. Adding weak bonds to the pure percolation case drastically reduces the dominance of the percolation-cluster backbone in the transport process. As $\kappa$ increases ($L_\kappa$ decreases) this effect becomes more important.

The models we used had a permeability ratio $\kappa = 0.004$, and we estimate the crossover length $L_\kappa$ as follows: We found an effective scaling exponent $D_c \simeq 1.5$, thus $L_\kappa \leq L$, since if $L\kappa \ll L$ we would see the characteristic scaling of DLA independent of the lattice geometry in simulations, and fourfold "snowflakes" in the experiments. Our experiments were also different from experiments on a percolation cluster [15]. We did not observe $D_c = 1.3$, and we may conclude that $L_\kappa$ is not much larger than $L$.

Referring back to Fig. 1, the model with $f \simeq 0.45$ is best described as homogeneous. Here the correlation length $\xi_l$ is small and permits averaging at the scale of the model. In addition, the low-permeability bonds form a homogeneous network with embedded clusters of good bonds. We therefore expect an effective scaling exponent $D \simeq 1.7$. At the other values of $f$ we have

$L_\kappa \sim \xi \sim R_g \sim L$ and scaling predictions seem futile.

We may visualize the aggregate as a collection of paths that live on clusters of good bonds, and that are linked to each other through weak bonds. In an experiment, a given pattern of paths is drained. Two length scales, $L_\kappa$ and $\xi_l$, participate in setting up such paths. We may think of $L_\kappa$ as a *path length* along good bonds, whereas $\xi_l$ is a *distance* between good bonds somehow connected. We have kept $L_\kappa$ constant as $\xi_l(f)$ was changed, and for $f \simeq 0.45$ it is reasonable to assume that $\xi_l \leq L_\kappa$ and that any connected path along good bonds on a cluster in that model will be shorter than $L_\kappa$. Qualitatively this means that within clusters only good bonds are used, the weak bonds are reserved for entering a new cluster.

In the models with higher values $f$, $\xi_l$ may increase indefinitely, giving long and tenuous paths (that scale with exponent 1.3) along good bonds within a cluster. However, if the path along an equipotential surface in the pressure field exceeds $L_\kappa$, a weak bond leading to radial growth will be preferred. Thus $L_\kappa$ is the dominating length scale in our models and limits the excursions of the paths for all $\xi_l(f) > L_\kappa$, i.e., we see no variation with $f$.

The arguments in the paragraphs above lead to the conclusion that the model geometries are in the middle of a crossover regime. Theory [13] makes us expect aggregates that have an effective fractal dimension intermediate to the limiting values 1.3 and 1.7. Since we find $D_c = 1.6$ in simulations on many models, the model size $L$ may be so large compared to $L_\kappa$ that we have almost homogeneous models. The fractal dimension we find is close to the value found for viscous fingering in random single-layered bead pack models, $D_c = 1.62$ [10]. Turning this argument around, these numbers could indicate the opposite: That random monolayer bead pack models are not quite homogeneous, but have a structure consisting of well connected regions embedded in a background of lower permeability (or vice versa), and that the fractal dimension $D_c = 1.62$ of VF in these models reflects the geometric structure in the model. The VF aggregates of Måløy and co-workers [10,21] look more like those obtained in our experiments and in the $401 \times 401$ simulations by Meakin *et al.* [13], than like ordinary DLA (on or off lattice). However, to resolve this question experiments on larger two-permeability models, where the crossover length $L_\kappa$ is well separated from the system size, are needed [22].

### D. Outlook

Experimental data are hard to acquire compared to generating data numerically. In future it may be possible to acquire experimental data with charge coupled device (CCD) cameras, which would eliminate the need to digitize film (an extremely laborious process). Then better statistics would become available by running experiments on many model realizations at chosen values of $\kappa$ and $f$. Presently CCD cameras that can acquire several pictures per second are not available. This rate, with a resolution of at least $2000 \times 2000$, is necessary for such experiments at high Ca.

In the future the effect of adding noise reduction [23] in the modified DLA algorithm we have used here could be studied. Considering the high overlap we obtain here, and the strong influence of the network on simulation results, we expect that the addition of some noise reduction will give a significant increase in overlap.

## V. CONCLUSIONS

For a system where the pore space had a percolation-cluster geometry [15], the displacement front was found to be fractal, with dimension $D = 1.3$. It was geometrically confined as it had to remain on the percolation-cluster backbone. In the present models the pore-space percolation geometry was modified by adding low-permeability bonds, and the displacement front geometry was strongly changed compared with viscous fingering on percolation-cluster geometry, and with viscous fingering on homogeneous models.

We fixed the permeability ratio at $\kappa = 0.004$, and varied the fraction $f$ of good bonds in the models, in the range $0.45 \leq f \leq 0.52$ close to the percolation threshold for bond percolation. For the values of $f$ tested, we found that the effective fractal dimension of both experimentally and numerically grown aggregates was $D_c \simeq 1.5$. We did not find the geometric crossover from $D = 1.3$ to 1.7 in the final aggregate as expected by Meakin *et al.* [13], but have observed a dynamic crossover from low-dimensional growth in early stages of the aggregates, to $D_c \simeq 1.5$ in the final aggregates.

Experimental and simulated crossover functions $F(x)$ were model dependent, but showed similar overall features when obtained on the same experimental models. We believe this is a consequence of the similarities in these networks. Crossover functions for simulations on different network realizations showed variations that were more pronounced than variations within a given model.

We found high experiment-simulation overlap, $S = 0.53$, for aggregates grown on the same model.

We could not find any systematic variations in overall scaling properties, crossover functions, or overlap that may be caused by variations in the fraction of high-permeability bonds.

The usually strong crossover with the correlation length $\xi(f)$ is suppressed by the presence of weak bonds. The weak bonds introduce a crossover length $L_\kappa \sim \xi < L$ that removes any variation with $\xi$ by short circuiting any path that makes tangential excursions of length greater than $L_\kappa$. Although weak bonds efficiently compete with good bonds, the models exhibit fractal VF displacement patterns that are strongly geometry dominated.

Meakin *et al.* [13] found a crossover from $D = 1.67$ at $f = 0.6$ to $D = 1.57$ at $f = 0.55$ for $\kappa = 0.0004$. Our results are consistent with their numerical findings, but can neither validate nor disprove these results. The experiments combined with simulations allow us to conclude that experiments are well described by simulations at the tested values of $f$ and $\kappa$. Simple modified DLA simulations described the observed fronts well, and showed the dependence on detailed pore geometry observed in the experiments. The algorithm provides a better characterization of the displacement process than merely giving a

fractal dimension, or presenting a crossover description based on averages over many runs.

## ACKNOWLEDGMENTS

One of us (U.O.) wishes to thank Alex Hansen for critical comments on the manuscript. We gratefully acknowledge support by VISTA, a research cooperation between the Norwegian Academy of Science and Letters and Den norske stats oljeselskap a.s. (STATOIL) and by NAVF the Norwegian Research Council for Science and the Humanities.

[1] B. B. Mandelbrot, *Fractals: Form, Chance, and Dimension* (Freeman, San Francisco, 1977).
[2] J. Feder, *Fractals* (Plenum, New York, 1988).
[3] T. Vicsek, *Fractal Growth Phenomena* (World Scientific, Singapore, 1989).
[4] P. G. de Gennes and E. Guyon, J. Mec. **17**, 403 (1978).
[5] R. Lenormand and C. Zarcone, Phys. Rev. Lett. **54**, 2226 (1985).
[6] D. Wilkinson and J. F. Willemsen, J. Phys. A **16**, 3365 (1983).
[7] T. A. Witten and L. M. Sander, Phys. Rev. Lett. **47**, 1400 (1981).
[8] J. D. Chen and D. Wilkinson, Phys. Rev. Lett. **55**, 1892 (1985).
[9] L. Paterson, Phys. Rev. Lett. **52**, 1621 (1984).
[10] K. J. Måløy, J. Feder, and T. Jøssang, Phys. Rev. Lett. **55**, 2688 (1985).
[11] R. Lenormand, E. Touboul, and C. Zarcone, J. Fluid Mech. **189**, 165 (1988).
[12] M. Eden, Proc. Berkeley Symp. Math. Sta. Probab. **4**., 223 (1961).
[13] P. Meakin, M. Murat, A. Aharony, J. Feder, and T. Jøssang, Physica A **115**, 1 (1989).
[14] J. Bear and Y. Bachmat, *Introduction to Modeling of Transport Phenomena in Porous Media* (Kluwer, Dordrecht, 1990).
[15] U. Oxaal, M. Murat, F. Boger, A. Aharony, J. Feder, and T. Jøssang, Nature (London) **329**, 32 (1987).
[16] U. Oxaal, Phys. Rev. A **44**, 5038 (1991).
[17] J. Feder, E. L. Hinrichsen, K. J. Måløy, and T. Jøssang, in *Fractals in Physics,* edited by A. Aharony and J. Feder (North-Holland, Amsterdam, 1989), pp. 104–111.
[18] P. Meakin and T. A. Witten, Phys. Rev. A **28**, 2985 (1983).
[19] M. Murat and A. Aharony, Phys. Rev. Lett. **57**, 1875 (1986).
[20] M. P. M. den Nijs, J. Phys. A **12**, 1857 (1979).
[21] K. J. Måløy, F. Boger, J. Feder, and T. Jøssang, in *Time-Dependent Effects in Disordered Materials,* edited by R. Pynn and T. Riste (Plenum, New York, 1987), pp. 111–138.
[22] A third explanation for $D_c = 1.6$ was proposed by Oxaal [16]. Standard DLA uses an outer boundary that is essentially at "infinity." This prevents the experimentally observed divergence of the growth near breakthrough.
[23] J. Nittmann and H. E. Stanley, Nature (London) **321**, 663 (1986).